European Conference on Computational Fluid Dynamics
ECCOMAS CFD 2006
P. Wesseling, E. Oñate and J. Périaux (Eds)

A GENERALIZED PATCH AMR PLATFORM THAT USES CELL CENTERED OR CELL VERTEX SOLVERS

Michel Borrel*, Juliette Ryan† and Germain Billet††

O.N.E.R.A.
BP 72, 92322 Châtillon cedex, France
*e-mail: michel.borrel@onera.fr
†e-mail: juliette.ryan@onera.fr
††e-mail: germain.billet@onera.fr

Key words: AMR Platform, Fluid Dynamics, Reacting Gas Flow, Combustion, MUSCL, DG, LES, Cavity Flow, Diffusion Flame

Abstract. *A patch adaptive mesh refinement (AMR) platform is presented. Presently two Navier-Stokes solvers are available within this platform : a MUSCL and DG solver (FLUX_AMR) and a multi-species MUSCL solver (MAJIC) for reacting flows. The first solver is based on cell centered approaches of finite volume type, the second solver is based on a cell vertex and a time splitting method. The modifications of AMR treatments, especially those concerning the interpolation at fine-coarse boundaries are detailed. This platform is first tested on the subsonic flow over a deep cavity and secondly on the interaction of a steady planar shock with a H2-air circular diffusion flame.*

1 INTRODUCTION

In fluid dynamics a large number of scales are present that must be resolved. Turbulent and reactive flows are typical examples in which scales in space remain confined in some regions while in time scales spread over many orders which makes very ill conditioned computational problems. In this work we have chosen the AMR method which is an adaptive refinement method in both space and time that is well suited to the physics. The idea is not to improve the accuracy locally but rather to gain computational time while keeping the same order of accuracy as using the globally refined grid. In fact, for complex multiscale 3D problems, the question is more how to make the computation possible with locally a large number of scales resolved in order to compute realistic physics. It appears that an AMR platform is more than a useful tool for computing complex flows : it can open the door to new computational strategies with less modelisation effort. In the literature, we generally find the AMR method associated with purely conservative approaches as this hierarchical method can be viewed as a multidomain non-conforming method in time and space and fine/coarse mismatch boundaries are easily treated with

fluxes. In 1999, ONERA started a research project on unsteady combustion. Its goal was to develop unsteady numerical tools such as AMR. The combustion solver with its complexity led us to adapt our AMR platform (previously associated with a classical MUSCL finite volume approach) to it, rather than to rewrite this solver. Thus the solver is used as a black box. The goal of this paper is to present and evaluate the AMR methodology on two typical complex flow problems handled in 2D in a first stage.

2 AMR

The local adaptive mesh refinement platform written at Onera by Borrel *et al* [1,2,3,4] from the originally method developed by Berger and Oliger [5], Colella [6], Quirk [7] and many other authors, uses a sequence of nested levels of refined structured patchwork grids, on which one or different solvers can be applied (Fig. 1). The patches are built around cells that have been flagged with a problem dependant sensor, using a grouping/clustering technique. On this hierarchy of grids, an unsteady grid cycling sequence is used (Fig. 2) which makes our coding completely non-recursive : coarse grids are advanced in time one step while fine grids are advanced multiple steps to reach the same time as coarse grids. All kinds of grid cycling can be used and, in order to save computer time for complex applications such as LES or combustion, the time synchronization could locally be relaxed at the finest level $lmax$, (under-resolved scales), but this possibility has not been tested in this study.

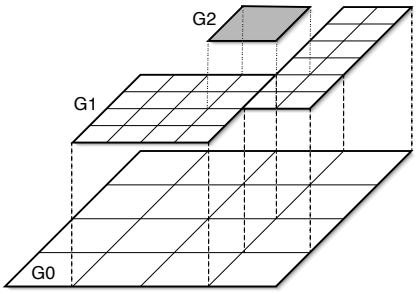

Figure 1: Hierarchical nested grids

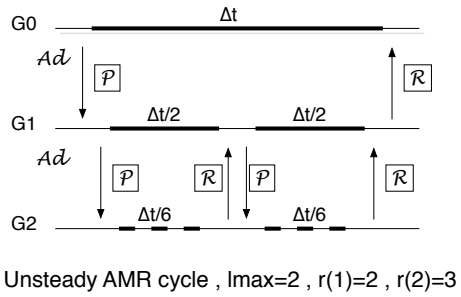

Figure 2: Grid cycling

The system of overlaid grids with successively finer and finer refinement, both in space and time, needs the following operators to couple the different levels:

1 - **Prolongation operator : $\mathcal{P}$**

This operator usually consists in retrieving and interpolating values from coarser patches.

2 - **Restriction operator : $\mathcal{R}$**

The second operator replaces coarse values by the overlying fine values using an averaging process or a least square technique.

3 - **Fine/fine boundary treatment :**

This interface operator, as the schemes used are entirely time explicit, is only coding work : it consists in retrieving computed values from neighbouring patches.

4 - **Fine/coarse boundary treatment :**

This point is the stumbling block of the AMR method. The treatment is dealt by creating around the fine patch a set of ghost cells or fictitious nodes with values interpolated from the coarse grid. The number of ghost cells/fictitious nodes per direction depends on the stencil of the scheme used and on the number of Runge-Kutta time steps done before updating AMR data set. Strong instabilities can arise from the choice of these interpolated values.

3 GOVERNING EQUATIONS

For a multicomponent gaseous (Ns species) reacting flow, the Navier-Stokes equations are written in the form

$$\begin{aligned}
\partial_t(\rho Y_i) + \nabla \cdot (\rho v Y_i) &= -\nabla \cdot (\rho Y_i V_i) + \omega_i,\ i \in [1, Ns] \\
\partial_t(\rho v) + \nabla \cdot (\rho v \otimes v) &= -\nabla \cdot \Pi \\
\partial_t(\rho e) + \nabla \cdot (\rho v e) &= -\nabla \cdot (q + \Pi v)
\end{aligned}$$

with

$$\Pi = pI - (\kappa - \frac{2}{3}\eta)(\nabla \cdot v)I - \eta(\nabla v + (\nabla v)^t), \quad (1)$$

$$q = \sum_{i \in S} \rho h_i Y_i V_i - \lambda \nabla T + p \sum_{i \in S} \chi_i V_i \quad (2)$$

$$\rho Y_i V_i = -\sum_{j \in S} \rho Y_i D_{ij}(d_j + \chi_j \nabla \log T) \quad (3)$$

$$d_i = \nabla X_i + (X_i - Y_i)\nabla \log p \quad (4)$$

where ∂_t and ∇ represent differentiation with respect to time and space, ρ denotes the density, Y_i and X_i the mass and mole fractions of the i^{th} species, $v = (v_x, v_y, v_z)$ the hydrodynamic velocity, V_i and ω_i the diffusion velocity and the mass production rate of the i^{th} species, $e = \frac{1}{2}v \cdot v + u$ the total energy per unit mass of the mixture where u is the internal energy per unit mass of mixture, T the absolute temperature, h_i the enthalpy per unit mass of the i^{th} species, p the thermodynamic pressure, q the heat flux vector, I the identity matrix and Π the pressure tensor. In this system of equations, the transport coefficients are expressed by

η : the shear viscosity

κ : the bulk viscosity
λ : the thermal conductivity
$D = (D_{ij})$: the diffusion matrix
$\chi = (\chi_i)$: the thermal diffusion ratios.
The system is closed by the equation of state

$$p = \rho RT \sum_{i \in S} \frac{Y_i}{M_i}$$

where R is the universal gas constant and M_i the molecular weight of the i^{th} species.

The expressions of the species diffusion velocities V_i and of the heat flux vector $q - \sum_{i \in S} \rho h_i Y_i V_i$ come from the kinetic theory of dilute polyatomic gas mixtures. All the transport coefficients are functions of the state of the mixture, as given by the variables p, T and Y_i.

These equations can be put in the compact form:

$$\partial_t W + \nabla \cdot F(W) = S \tag{5}$$

where W is the conservation variable vector, F the flux vector (inviscid and viscous part) and S the source term associated to the chemistry. For non reactive flows, $S = 0$.

4 SOLVERS

The AMR platform is based on a cell technology, independent of the solver which can be either a cell centered or a cell vertex formulation.

4.1 CELL CENTERED SOLVER

Following the works of Van Leer, Roe, Cockburn and many others authors, MUSCL and DG are now classical methods to solve conservation law equations. In FLUX_AMR the two approaches MUSCL and DG-P^1 are implemented for perfect non reacting gas. Although their formulation is similar, their behavior differs completely.

4.1.1 Weak formulation :

At each time $t \in [0, t_f]$, an approximate solution $\mathrm{W}_h(x, y, z, t)$ is computed from an initial solution $\mathrm{W}^0(x, y, z)$ and boundary conditions. The computational 3D domain Ω is partitioned using an i, j, k structured mesh. The centre of each cell Ω_{ijk} is noted $x_{O_{ijk}}, y_{O_{ijk}}, z_{O_{ijk}}$. In each cell, the solution is expanded on a local basis of degree one polynomials:

$$\forall (x, y, z) \in \Omega,\ \forall t \in [0, t_f],\ \mathrm{W}_{h(x,y,z,t)} = \sum_{i,j,k} \Big(\sum_{\ell=0,3} p^{\ell}_{ijk}(x, y, z) \bar{\mathrm{W}}^{\ell}_{ijk}(t) \Big) \tag{6}$$

where $\{p^{\ell}_{ijk},\ \ell = 0,3\}$ is the local basis of Legendre first order polynomials :

$$\left\{\begin{array}{lcll} p^0_{ijk}(x,y,z) & = & 1 & \text{if } (x,y,z)\in\Omega_{ijk},\ \ 0 \text{ else} \\ p^1_{ijk}(x,y,z) & = & x - x_{O_{ijk}} & \text{if } (x,y,z)\in\Omega_{ijk},\ \ 0 \text{ else} \\ p^2_{ijk}(x,y,z) & = & y - y_{O_{ijk}} & \text{if } (x,y,z)\in\Omega_{ijk},\ \ 0 \text{ else} \\ p^3_{ijk}(x,y,z) & = & z - z_{O_{ijk}} & \text{if } (x,y,z)\in\Omega_{ijk},\ \ 0 \text{ else} \end{array}\right. \tag{7}$$

$\bar{\mathrm{W}}^{\ell}_{ijk}$ are the degrees of freedom on Ω_{ijk} which approximate the mean and gradient cell values. In both approaches, the discretization is built from the weak formulation of (5) obtained by multiplying by a test function φ_h in a space V_h and by integrating by parts on Ω (with $S = 0$):

$$\int_{\Omega_{ijk}} \varphi_{ijk}\frac{\partial}{\partial t}\mathrm{W}_h d\Omega + \oint_{\partial\Omega_{ijk}} \varphi_{ijk}\tilde{\mathbf{F}}(\mathrm{W}_h)\cdot\overrightarrow{\mathbf{n}}\, d\sigma - \int_{\Omega_{ijk}} \nabla\varphi_{ijk}\cdot\mathbf{F}(\mathrm{W}_h)d\Omega = 0 \tag{8}$$

with :

$$V^n_h \ = \ \{\varphi_h \ \in \ L^1(\Omega)\ /\ \forall(i,j,k),\ \varphi_h|\Omega_{ijk} \ = \ \varphi_{ijk} \ \in \ P^n(\Omega_{ijk})\} \tag{9}$$

where $P^n(\Omega_{ij})$ represents the polynomials of degree at least n on Ω_{ijk}. For DG, we take $n = 1$ and for MUSCL $n = 0$ (finite volume approach). The choice of Legendre polynomials as basis leads to the ODE system :

$$\left\{\begin{array}{rcl} \dfrac{d}{dt}\bar{\mathrm{W}}^0_{ijk}\displaystyle\int_{\Omega_{ijk}} d\Omega & = & -\displaystyle\oint_{\partial\Omega_{ijk}} \tilde{\mathbf{F}}\cdot\overrightarrow{\mathbf{n}}\, d\sigma \\ \dfrac{d}{dt}\displaystyle\sum_{l=1,3}\left(\bar{\mathrm{W}}^l_{ijk}\int_{\Omega_{ijk}} p^l_{ijk}\, p^m_{ijk} d\Omega\right) & = & -\displaystyle\oint_{\partial\Omega_{ijk}} p^m_{ijk}\tilde{\mathbf{F}}\cdot\overrightarrow{\mathbf{n}}\, d\sigma + \int_{\Omega_{ijk}} \mathbf{F}\cdot\nabla p^m_{ijk}\, d\Omega \\ & & (m = 1,2,3) \end{array}\right. \tag{10}$$

This ODE is classically solved using a RK2 time discretisation. For MUSCL, only the first equation is relevant and for DG, if a Cartesian grid is used, the mass matrix of the second equation is diagonal.

4.1.2 Slope reconstruction and slope limitation :

Introducing slope limiters that ensure stability but doesn't degrade the accuracy of the method is a crucial issue in both approaches. For wave propagation problems, this is efficiently done with MUSCL and the *triad* limiter introduced in Billet *et al* [8]. Limiting the slopes for DG-P1 with these limiters consists in taking the *Minmod* value between the corresponding degrees of freedom and gradients calculated with the limiter in each grid direction (ξ). In the case of a Cartesian grid, this can be written :

$$\bar{\mathrm{W}}^{\ell,triad} \ = \ Minmod(\,\bar{\mathrm{W}}^{\ell}\,,\,\Delta^+_{\ell}/\Delta\xi\,,\,\Delta^-_{\ell}/\Delta\xi\,)\ \ ,\ \ell = 1,3 \tag{11}$$

4.1.3 Flux integral computation :

Three types of flux integrals are to be computed with DG and only one with MUSCL :

$$\oint_{\partial\Omega_{ijk}} \tilde{\mathbf{F}} \cdot \overrightarrow{\mathbf{n}} d\sigma \ , \ \oint_{\partial\Omega_{ijk}} p^m_{ijk} \tilde{\mathbf{F}} \cdot \overrightarrow{\mathbf{n}} d\sigma \ \text{ and } \int_{\Omega_{ijk}} \mathbf{F} \cdot \nabla p^m_{ijk} \, d\Omega \tag{12}$$

In the first two integrals, $\tilde{\mathbf{F}}$ represents numerical fluxes defined at interfaces from upwind and downwind values W_h^R et W_h^L. With MUSCL, only one numerical flux evaluation is done by interface during a time step and with DG, four evaluations using a four point Gaussian quadrature. The volume flux integrals (third type) are evaluated using an eight Gaussian point quadrature. Concerning the numerical flux formulas used, the inviscid part is treated with different flux formulas (classically Roe or $AUSM^+$ for MUSCL, Roe or Lax-Friedrich for DG). The viscous part is treated with a reconstruction viscous gradient technique (Cf. Borrel *et al* [9,10] for DG).

4.1.4 AMR fine/coarse boundary treatment :

Fine boundaries are computed by evaluating fine fluxes using ghost values interpolated from the underlying coarse cells. And then, for MUSCL, the underlying coarse fluxes are corrected by readjusting interface fluxes (see Fig.3). This correction can be written in the following way:

$$\mathrm{W}^{corr}_{IJK-1} = \mathrm{W}_{IJK-1} - \frac{\delta t}{\delta x} \left[\Sigma_r \mathcal{F}^{fine}(\mathrm{W}_{ghost}, \mathrm{W}_{ijk}) - \mathcal{F}^{coarse}(\mathrm{W}_{IJK-1}, \mathrm{W}_{IJK}) \right] \tag{13}$$

where $\mathcal{F}$ is the numerical flux and r the refinement ratio. This correction has not yet been extended for DG which is not a genuinely conservative approach. For LES applications, following Quéméré [11], a correction is added to the interpolated ghost values which corresponds to a frequency complement evaluated in the coarse adjacent cell :

$$\mathrm{W}_{ghost} \ = \ \mathcal{P}_{IJK-1}(X_{gh}) \ + \ \mathcal{C} \left(\mathrm{W}_{ijk} \ - \ \mathcal{P}_{IJK}(X_{ijk}) \right) \tag{14}$$

where $\mathcal{P}_{IJK}(X)$ is an interpolation defined in coarse cells and $\mathcal{C}$ a relaxation constant taken equal to 0.7. An interpolation in time should also be introduced.

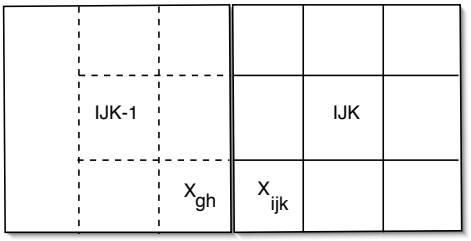

Figure 3: Cell centered solver: ghost cells schematic description

4.2 CELL VERTEX SOLVER

A 3D code (MAJIC) to solve unsteady reactive flows has been developed. It uses the time-splitting method proposed in the 50^{th} by American and Russian research teams (Douglas, Peaceman, Rachford, Yanenko, D'Yakonov, Samarskii, ...) and improved since then by many researchers. The mathematical foundations have been presented in the Lions and Temam's works [12] and Laval's papers [13]. The 3-D finite difference operator is split into a product of simpler explicit operators:

$$W_j^{n+2} = (\pounds_H \pounds_P \pounds_S \pounds_P \pounds_H)\, W_j^n \tag{15}$$

where $\pounds_H$, $\pounds_P$ and $\pounds_S$ are the operators associated with the hyperbolic, parabolic and source terms of the Navier-Stokes equations. This splitting allows the different parts of the NS equations to be solved with specific algorithms or specific hypotheses. Recently, a simple model called 'double flux model' preserving the pressure and the velocity across the contact discontinuities has been proposed by Abgrall and Karni[14]. It has been extended to the reactive flows composed with species whose constant pressure heat capacities C_{p_i} depend on the temperature, by Billet and Abgrall[15]. This model is taken into account in operator $\pounds_H$. All the diffusion and dissipation terms (operator $\pounds_P$) are solved with a 3D centered second-order scheme. In operator $\pounds_S$, a detailed chemical reaction mechanism for $H_2 - Air$ flames is considered.

Generally, operator $\pounds_H$ solves the most difficult part of Navier-Stokes equations because of the presence of strong nonlinear phenomena in the flow and a particularly attention has been done for its resolution. 3D operator $\pounds_H$ is split into 1D operators $\pounds_{H_\alpha}$ (where α represents each direction x, y and z). For these convective terms, adaptive limiters introduced in a MUSCL procedure have been proposed. Their compressive properties suitably balance the diffusive effects of $AUSM^+$ flux splitting[16], and allows to obtain

numerical solutions quasi exempt of numerical instabilities while minimising the numerical dissipation[8]. When the pressure fluctuations are not negligible (turbulent flows for instance), we apply a triad of limiters. In $\pounds_{H_\alpha}$, the stencil uses five nodes $(j-2, ..., j+2)$ and the values at these nodes allow to compute the wave length associated with the local evolution of the variables and to choose the appropriate expression of limiter. When the local variation is monotone, a third-order uncentered scheme is called. But for avoiding to inhibit the energy cascade too quickly, we use a centered reconstruction for high wave numbers. Finally, a Godunov scheme is applied for the highest wave numbers in order to attenuate the numerical instabilities. When the pressure fluctuations are weak, a specific limiter is chosen in order to describe correctly the convection of quantities. This limiter depends on two parameters which are chosen in order to minimize the lower-order error terms of the equivalent system[17].

The simulations are performed with a one time step scheme (Euler's scheme) for all the operators. With Euler's scheme, the equivalent system can still be obtained and studied even in the regions where the variations of the quantities are strong. This allows a better control of the error terms than with a multistep algorithm because with this type of algorithm the equivalent system becomes too intricate to obtain an objective information of the diffusive and dispersive properties of the scheme. The one time step scheme also has the advantage in reducing the number of elementary operations and thus computational cost.

If we assume that the results obtained for a convection-diffusion equation are still valid for the Navier-Stokes equations[17], the Navier-Stokes equivalent system is stable and is a second-order approximation of the Navier-Stokes equations if the time step verifies

$$\delta t \leq Min\left[\delta t_H, \delta t_P, \delta t_S\right] \tag{16}$$

where δt_H, δt_P and δt_S are time steps associated with the operators $\pounds_H, \pounds_P$ and $\pounds_S$ with

$$\begin{aligned}
\delta t_H &\leq Cfl\ Min_{\alpha,j}\left\{\frac{\Delta\alpha}{|v_\alpha|+c}\right\} \\
\delta t_P &\leq Min\left[Min_{\alpha,j}\left(\frac{\rho C_v \Delta\alpha^2}{6\lambda}\right), Min_{\alpha,j}\left(\frac{14\rho\Delta\alpha^2}{3\eta\left[8+\Delta\alpha^2(\frac{1}{\Delta\beta^2}+\frac{1}{\Delta\gamma^2})\right]}\right)\right], \gamma\neq\beta\neq\alpha.
\end{aligned}$$

c is the celerity of sound and C_v the specific heat at constant volume of the mixing (to obtain the previous condition, C_v is assumed constant). When a detailed chemical scheme is used, the time step δt_S is driven by some reactions. In practice, δt_S is bounded by the maximum variation of some species production during a time step given by empirical criteria. Generally, in the applications, condition (16) reduces to $\delta t \leq \delta t_S$. If $\Delta\alpha = \Delta x = \Delta y = \Delta z$, this last constraint on δt gives a condition on the mesh size based on the Courant and Fourier criterion

$$\Delta x \geq Max\left[\frac{Max_{\alpha,j}(|v_\alpha|+c)\delta t_S}{Cfl}, \sqrt{Max_j(\frac{6\lambda}{\rho C_v})\delta t_S}, \sqrt{Max_j(\frac{15\eta}{7\rho})\delta t_S}\right] \tag{17}$$

in order that the global scheme (15) remains a second-order scheme. When the acoustic phenomena are negligible we take $Cfl \leq 0.5$ otherwise $Cfl \leq 0.1$.

This code has been evaluated on numerous published flow simulations. It gives results as accurate as high order methods (ENO, MENO, WENO, Hermitian, pseudospectral, ACM with wavelet filter schemes, sixth-order centered explicit schemes with fourth-order Runge-Kutta algorithm) [8,15,17,21,22].

4.2.1 AMR fine/coarse boundary treatment :

With cell vertex solvers even conservative ones, this boundary treatment cannot be completely conservative as we are in a nodal strategy as opposed to a cell strategy. The interpolation developed is such that coarse and fine values as well as their gradients coincide at the fine coarse interface. Second order centered coarse gradients are computed at each adjacent coarse cells:

$$\frac{\partial W^{coarse}}{\partial x}\Big|_J^N, \frac{\partial W^{coarse}}{\partial x}\Big|_{J-1}^N, \frac{\partial W^{coarse}}{\partial x}\Big|_J^{N+1}, \frac{\partial W^{coarse}}{\partial x}\Big|_{J-1}^{N+1} \tag{18}$$

and then by a Q1 interpolation the quantities $G_j^k = \frac{\partial W^{coarse}}{\partial x}\Big|_j^k$ are evaluated at each fictitious node j and for each sub-time level k, see Fig.4 . Fine values at fictitious nodes are then determined successively so that second order centered fine gradients match the computed coarse gradients.

$$W_{j-1}^{fictitious,k} = W_{j+1}^{fine,k} - 2\,\delta x\, G_j^k \tag{19}$$

δx is the fine space step. Once the fine solver has finished its advance in time, the underlying coarse values are replaced by the fine ones, the difference between fine values and pre-computed coarse values being of the order of the discretisation error. This boundary restriction operator has been shown to be the most stable.

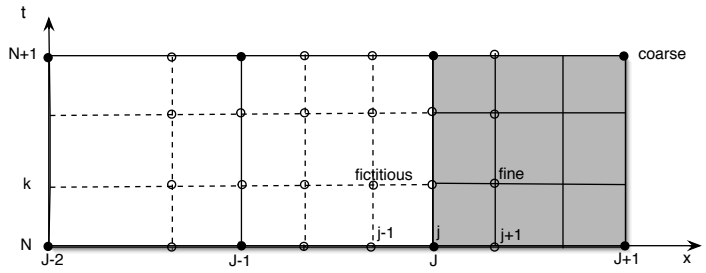

Figure 4: Cell vertex solver: schematic of the stencil and time-space fictitious points

For the cell vertex solver, interface points are treated as if they were inner points. Values computed by the solver at fictitious nodes will be discarded during the integration of the fine patch within the coarser grids.

5 COMPUTATIONAL RESULTS

In this section the objective is first to validate the different numerical procedures introduced on two problems geometrically simple but with complex physics and then, to identify the advantages one can take using the AMR platform.

5.1 SUBSONIC FLOW OVER a CAVITY

The test case retained for FLUX_AMR, as academic problems have already been carried out and published, is the flow over a deep cavity ($L/D = 0.42$) open in a channel at free-stream Mach number 0.8, see Fig 9 left. The Reynolds number based on the length $L = 50mm$ of the cavity is $Re_L = 7.10^5$. The incoming boundary layer on the upper and bottom walls are fully turbulent. An experimental database is available (Cf. Forestier-Jacquin [18]) and an extensively computational study has been performed (Cf. Larchevêque *et al* [19] with structured grids or Bertier [20] with unstructured grids). Strong self-sustained pressure oscillations and traveling waves take place inside the flow with a complex but mainly two-dimensional organisation. This cavity flow problem is particularly well suited for our evaluation. First, a 2-D hypothesis allows, in a first step, to save memory and CPU time for a numerical comparison of different approaches. And secondly, the multi-

scale phenomenology with the local viscous effects in one hand, the large eddy structures in the shear layer and the global acoustic waves in the other hand can be efficiently handled by the AMR strategy. The computations have been performed in 3D with an degenerated direction. The computational domain reproduces the exact geometry in 2D of the surrounding domain part of the wind tunnel of the experiment. No turbulence modeling has been introduced in the computation (MILES approach) as we are concerned here mainly by the propagation of the instabilities and the coherent structures inside the shear layer.

5.1.1 Characteristics of the flow

The flow is governed by a feedback mechanism between the shear layer which takes place on the open side of the cavity and the acoustics produced by the breakdown of the three vortex structure impinging periodically the downstream corner of the cavity (Fig. 5). This complex mechanism results in upstream traveling waves which must be numerically smeared out at the inflow boundary.

5.1.2 Initial and boundary conditions

Computations are started with a double boundary layer profile evaluated from experiment, which is uniformly reproduced in all the cross sections of the channel :

$$\left\{ \begin{array}{lcl} \rho/\rho_\infty & = & 1\,/\,[1\,+\,0.128\,(1-(u/u_\infty)^2)] \\ u/u_\infty & = & [tanh(6.7708\,y/L)]^{0.128828} \end{array} \right. \tag{20}$$

and with stagnation conditions inside the cavity. At $t = 0$ the upper side of the cavity is open. At the outflow boundary, prescribed static pressure (64600 Pa) is imposed; on solid walls, adiabatic conditions and, at the inflow boundary, non reflecting conditions are taken.

5.1.3 Mesh strategy

The AMR grids are built with a geometrical progression in the span-wise and the normal channel wall directions : in order to avoid non fitting refined interface nodes, all the coordinates are stored at the beginning of the computation. Three levels of embedded grids have been used (Fig. 6): the coarser one (basic grid) corresponds to the acoustics, the finer one to the inner boundary layer which develops near channel walls with $y^+ \approx 10$ and the medium one which corresponds to the large eddies.

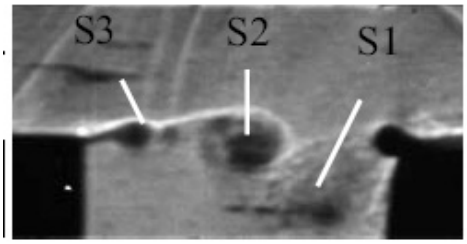

Figure 5: Cavity flow : instantaneous view of the shear layer (density values) from an experimental set-up.

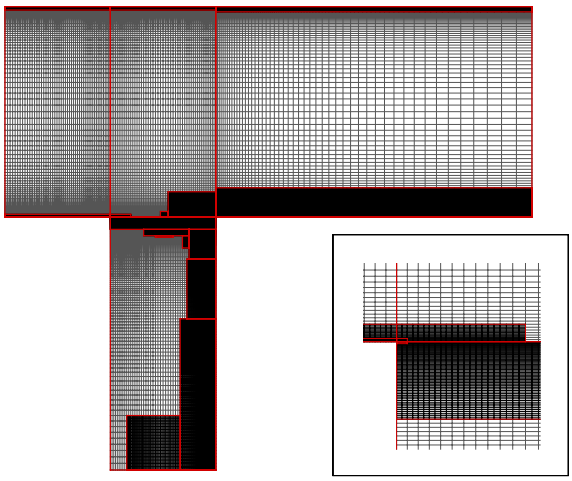

Figure 6: Cavity flow : instantaneous patch Cartesian grids

The globally refined grid is made of about 2 million cells (with two cells along the degenerated direction) and the AMR strategy allows us to work with only 180000 cells. The frequency complement treatment (eq. (14)) has been used for the finer level with MUSCL but this procedure doesn't work presently with DG. In our computation, only the medium grid is adaptive with a refinement indicator built with the entropy levels; it would probably have been possible to obtain good results with all the grids fixed once, but our objective here was first of all to evaluate all the AMR operators.

5.1.4 MUSCL and DG results

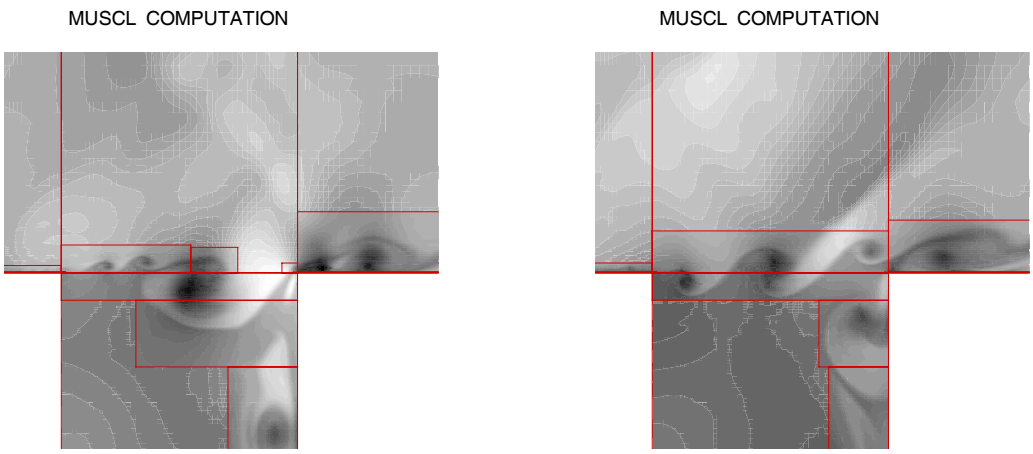

Figure 7: Cavity flow : instantaneous view of the shear layer (density values) at two different times.

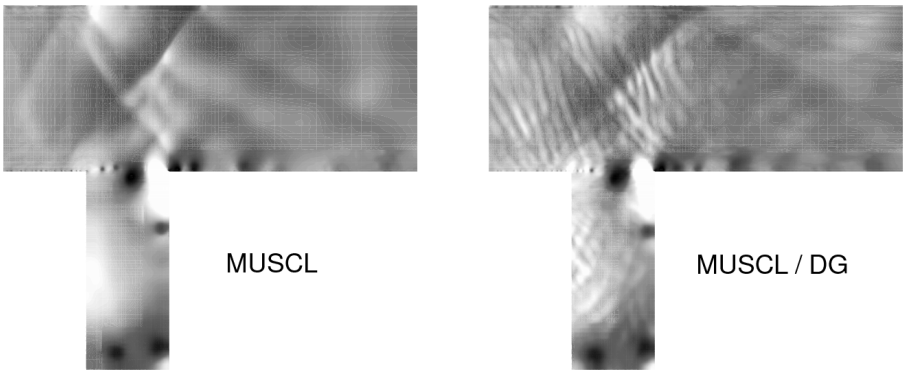

Figure 8: Cavity flow : instantaneous pressure flowfields (MUSCL and MUSCL/DG results).

Three computations have been carried out : the first one with MUSCL (AUSM+) used on each level, the second one with DG and the third one with DG used on the basic level and MUSCL on the two refined levels. The second computation has lead to instabilities inside the shear layer which cannot be controlled even adding a Smagorinsky model. The instabilities of DG could be controlled using the Lax-Friedrich fluxes and a very diffusive limiter but with very smeared results. In terms of efficiency, the coupled MUSCL/DG computation requires 2.5 times more CPU time as the MUSCL one, essentially due to CFL constraint and the DG computation 4 times more. The main characteristics of the flow are reproduced in the MUSCL computation (Fig. 7).

If we compare the pressure flowfield of MUSCL and MUSCL/DG computations (Fig. 8), we see that the low frequency waves compare rather well but high frequency acoustic waves appear only in the results of MUSCL/DG computation : numerical or physical origin of this discrepancy has not clearly been analysed.

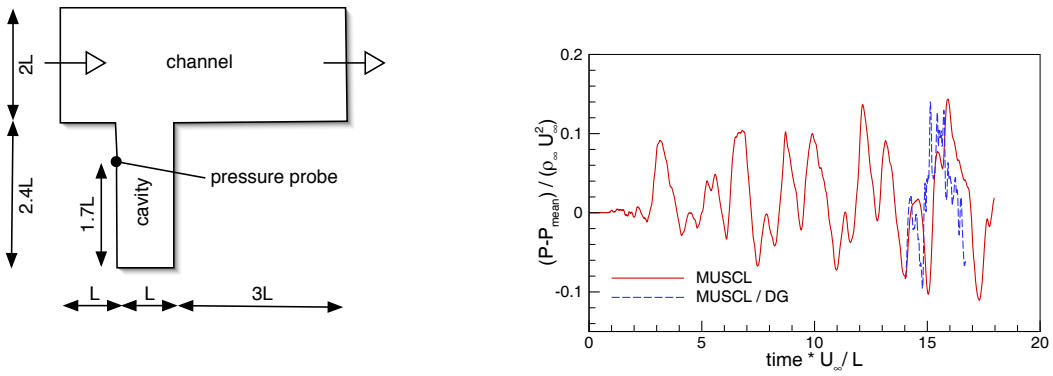

Figure 9: Cavity flow :Left) schematic description of the computational domain. Right) pressure signals from the probe (MUSCL and MUSCL/DG results).

The signals obtained from the numerical pressure probe located on the wall of the cavity indicate that we are still within the transition phase : the periodic regime is not yet reached, so no comparison with the cited experimental or numerical results (3D) can be made at that stage. The MUSCL computation required 20000 explicit iterations and about 10 CPU hours on a NEC computer. The MUSCL/DG computation started from the previous results at iteration 12000 and for only 4000 iterations and 2h30 CPU. The main frequency of the phenomenon is located at about 1500Hz for the MUSCL computation and at 2000Hz for the MUSCL/DG computation, which is closer to the experimental data but we need to continue further the computations to validate this tendency.

5.2 DIFFUSION FLAME-SHOCK WAVE INTERACTION

The conservative form of the equations also allows to do simulations of flows in which shock waves may appear. For example, the behavior of a circular-section diffusion flame at the crossing of a shock is an interesting topic. Understanding the conditions under which the vortices, forming after the interaction, play a major role in the increase in flame surface and consequently in the reduction of complete combustion time remains an open question. This test case is presented in [23]

5.2.1 Characteristics of the flow

The time duration between the moment when the reactions begin to appear and the time when the flame goes through the shock as well as the temperature and the fuel concentration within the flame have an influence on the thickness of the mixing layer and on the location and the intensity of the vortices and consequently on the combustion efficiency. In this flow, the two counterrotating vortices completely wrap around part of the flame, but as this region contains practically no oxygen, they do not manage to bring the fuel and the oxidiser into contact in proportions sufficiently close to the stoichiometric ratio and with a temperature sufficiently high to trigger the reactive processes.

5.2.2 Initial and boundary conditions

At $t_0 = 0$, a circular bubble filled with H_2 ($Y_{H_2} = 0.233$) and N_2 ($Y_{N_2} = 0.767$) species begins to diffuse in the ambient air. The temperature is $300K$ in the bubble and $1500K$ in the air. The pressure is uniform and equal to 1 atm. The radius of the circular flame just before reaching the shock is $1.7mm$. A circular diffusion flame begins to set up and at $t_2 = 1.6\ 10^{-4}s$, this flame hits a Mach 2 planar shock. At this time, the size of the computational domain is $0 \leq x \leq 10mm$ and $0 \leq y \leq 5mm$ and the mesh size is $\Delta x = \Delta y = 25\mu m$ (this value respects the condition (16) with $Cfl = 0.1$). A reflection boundary condition is applied at $y = 0$ and Neumann conditions at $y = 5mm$. NSCBC conditions are used at $x = 30mm$. The chemical mechanism involves nine species (H_2, O_2, H_2O, H_2O_2, HO_2, OH, H, O, N_2) and 38 elementary reactions[24]. Nitrogen is assumed inert. Time step δt is driven by the chemical reactions and more particularly by the production criteria of species Y_{HO_2} and $Y_{H_2O_2}$ and during the computation, $10^{-11}s \leq \delta t \leq 5\ 10^{-10}s$. For this simulation, the Reynolds number linked with the main vortex size and its induced velocity is $Re_{vortex} \approx 2800$. The Damköhler number calculated from the time associated with the vortex and the characteristic chemical times of the faster and slower reactions is $0.1 \leq Da \leq 10000$. The Kolmogorov scale based on the width of the domain and the characteristic values of the flow behind the shock is $\eta_k \approx 2.5\mu m = \frac{\Delta x}{10}$. The barodiffusive effect, Soret effect and the binary diffusion coefficients are taken into account but Dufour effect and the bulk viscosity are neglected (the influence of this last transport coefficient is presented in [25].

5.2.3 Mesh strategy

Results are shown with and without AMR strategy. For the AMR computation, the initial coarse mesh is a regular 201 x 101 mesh. Two levels of embedded grids have been used. Patches are defined using a sensor based on the gradient of all primitive variables. Any cell that has a gradient that is over 15% of the maximum value is refined. These patches are redefined every 50 time steps (see Fig. 10). Computations without AMR are made on the fully refined AMR coarse mesh.

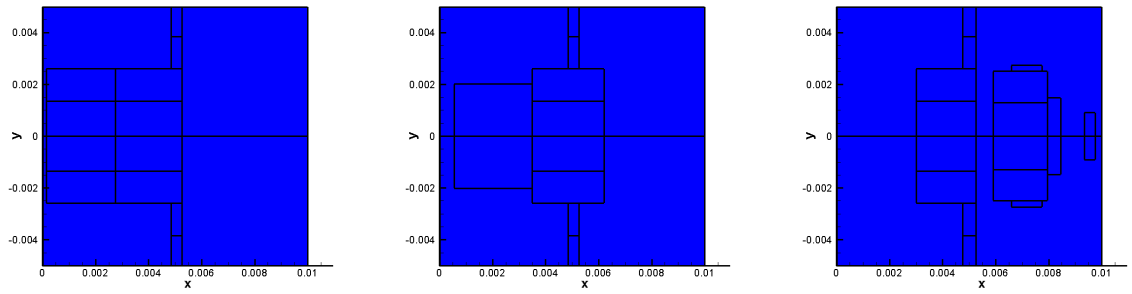

Figure 10: Flame shock interaction: AMR patches time evolution

5.2.4 Results

Results are shown without and with AMR strategy. Computations with AMR are 4 times less expensive in CPU time with a memory storage divided by 3. There is very little difference between the two computations. As one can see on results with AMR the sensor that flags areas to be refined could be better adjusted, (i.e. zones of little interest are still being flagged). This definition of the sensor is very much problem dependent and still requires quite a know-how of the physical phenomena being studied.

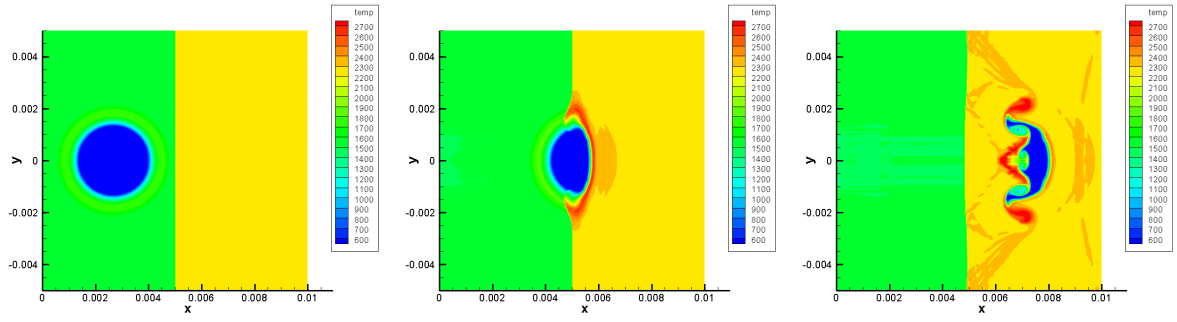

Figure 11: Flame shock interaction - without AMR: Temperature evolution through the shock

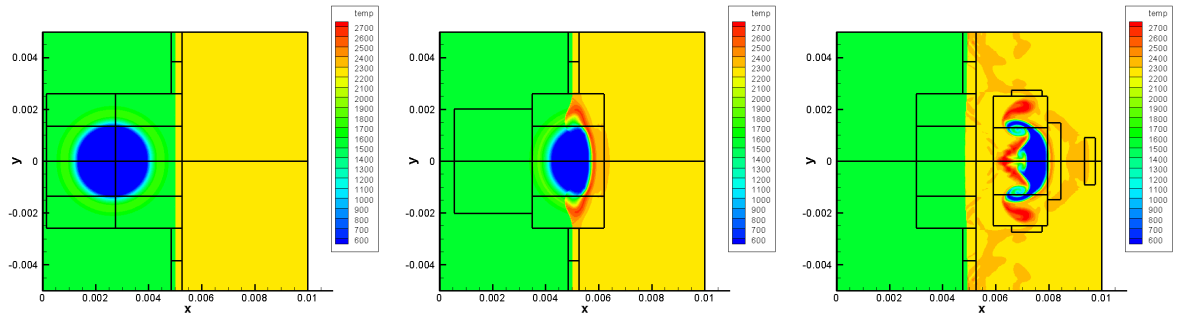

Figure 12: Flame shock interaction - with AMR: Temperature evolution through the shock

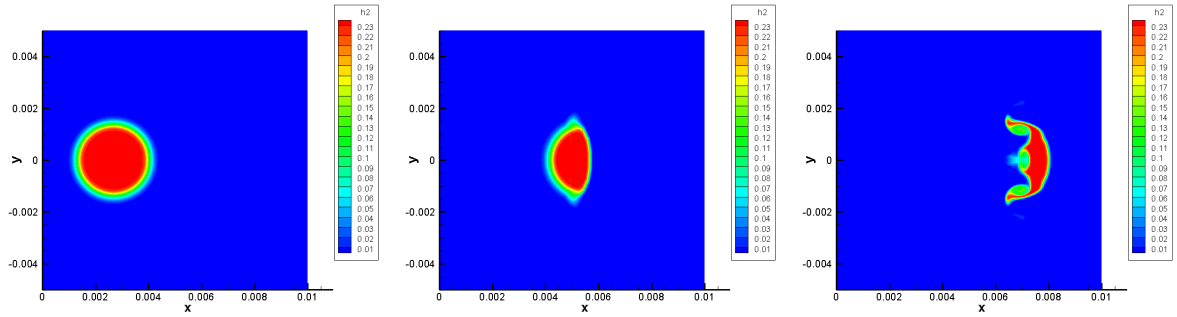

Figure 13: Flame shock interaction - without AMR: Y_{H_2} evolution through the shock

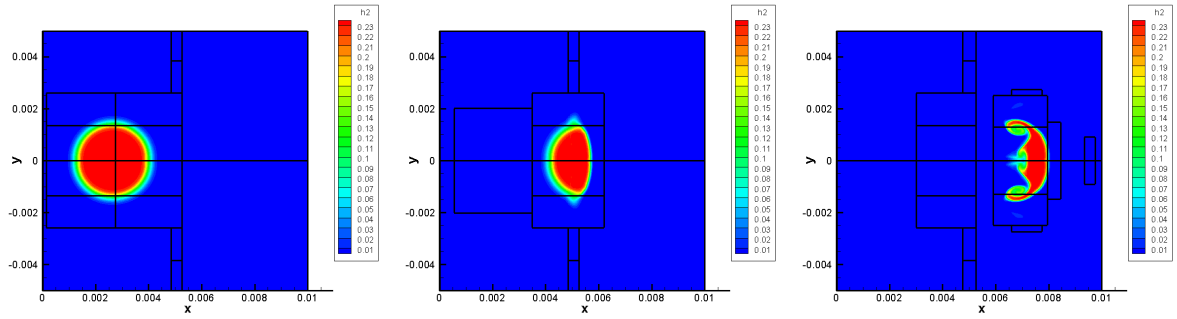

Figure 14: Flame shock interaction - with AMR: Y_{H_2} evolution through the shock

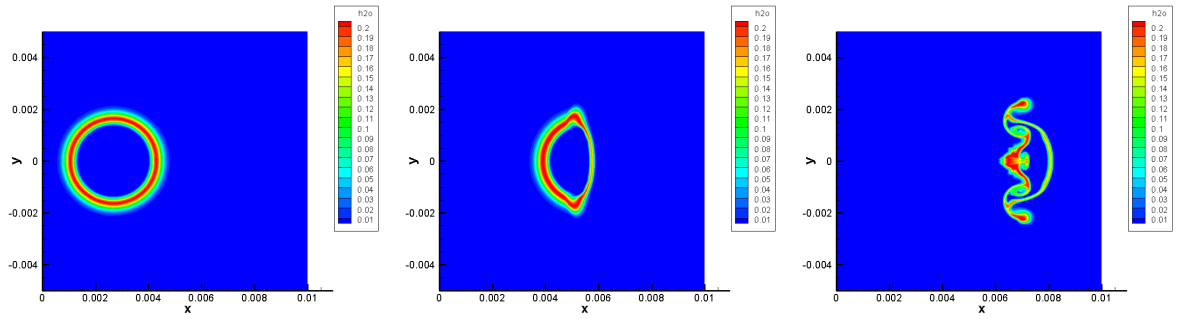

Figure 15: Flame shock interaction - without AMR: Y_{H_20} evolution through the shock

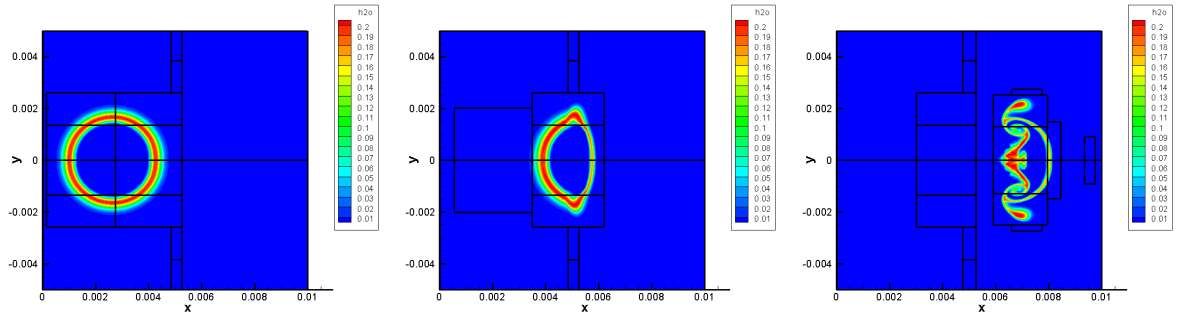

Figure 16: Flame shock interaction - with AMR: Y_{H_20} evolution through the shock

6 CONCLUSIONS

Our approach to adaptive gridding used here has proved to be successful with either cell centered or cell vertex gas dynamics second order solvers. The challenge for reacting gas flows was to devise numerical procedures which could capture discontinuous flow features without introducing non-physical oscillations into the solutions (oscillations that could be very unstable and emphasize artificially the reactive phenomena). Work is still to be done with a theoretical and numerical validation to see whether the developed fine/coarse treatments remain always stable.

The AMR platform presented is written in standard FORTRAN and, even if some work remains to be done to optimize the coding, for example concerning dynamic memory allocation or high performance parallel computation, the perspectives for computing very complex multi-scale 3D flows are quite good. The physical models can be adapted with the level of refinement : Euler/Navier-Stokes, mono/multi-species, empirical laws/detailed transport mechanisms, global/detailed chemical scheme,... As all the coding is in 3D, this extension will only be a question of computing resources. Although curvilinear grids can be used with the AMR methodology, the three computations presented here with Cartesian grids have shown some of the possibilities of this refinement method.

REFERENCES

[1] J.-C. Jouhaud and M. Borrel. *Discontinuous Galerkin and MUSCL strategies for an adaptive mesh refinement method,* Proceedings of the 15^{th} ICNMFD, Monterey, *Springer Ed.*, 400–405, (1996).

[2] J.-C. Jouhaud and M. Borrel. *A hierarchical adaptive mesh refinement method : application to 2D flows*, 3^{rd} ECCOMAS CFD Conf., (1996).

[3] N. Huré and M. Borrel. *A multiblock multigrid AMR method using a MUSCL or a Discontinuous Galerkin approach*, Finite Volumes for Complex Applications III, Hermes Penton Ltd, (2002).

[4] J. Ryan and M. Borrel. *Adaptive Mesh Refinement : a coupling framework for Direct Numerical Simulation of reacting gas flow*, ICFD, Oxford, (2004).

[5] M.J. Berger , J. Oliger. *Adaptive Mesh Refinement for Hyperbolic Partial Differential Equations*, J. Comput. Phys.,**53**, 484–512, (1984).

[6] M.J. Berger and P. Colella. *Local Adaptive Mesh Refinement for Shock Hydrodynamics*, J. Comput. Phys., **82**, 64–84, (1989).

[7] J.J. Quirk. *An adaptive grid refinement algorithm for computational shock hydrodynamics*, PhD thesis, Cranfield Institute of Technology, (1991).

[8] G. Billet, O. Louédin. *Adaptive limiters for improving the accuracy of the MUSCL approach for unsteady flow*, J. Comput. Phy., **170**, 161–183, (2001).

[9] M. Borrel, B. Berde. *Moment approach for the Navier-Stokes equations*, AIAA paper 95-1663, 12^{th} CFD Conf., San Diego, (1995).

[10] C. Drozo, M. Borrel, A. Lerat. *Discontinuous Galerkin schemes for the compressible Navier-Stokes equations*, Proceedings of the 16^{th} ICNMFD, Arcachon, *Springer Ed.*, 266–271, (1998).

[11] P. Quéméré, P. Sagaut, V. Couaillier. *A new multi-domain multi-resolution method for large -eddy simulation*, Int. J. Numer. Meth. Fluids, **36**, 391–416, (2001).

[12] J.L. Lions, R. Témam. *Une méthode d'éclatement des opérateurs et des contraintes en calcul des variations*, C. R. Académie des Sciences, **263**, 563–565, (1966).

[13] P. Laval *New splitting-up schemes for solving hyperbolic and parabolic non linear problems: applications to Euler and Navier-Stokes equations*, Recherche Aérospatiale, **4**, 257–309, (1983).

[14] R. Abgrall , S. Karni. *Compressible multifluids,* J. Comput. Phys., 169, pp594-623, (2001).

[15] G. Billet, R. Abgrall. *An adaptive shock capturing algorithm for solving unsteady reactive flows*, Computers and Fluids, **32**, 1473–1495, (2003).

[16] M.S. Liou. *A sequel to AUSM: AUSM$^+$,* J. Comput. Phys., 129, (1996).

[17] G. Billet. *Improvement of convective concentration fluxes in a one step reactive flow solver*, J. Comput. Phys. **204**, 319–352, (2005).

[18] N. Forestier, L. Jacquin, P.Geffroy. *The flow-field over a deep cavity at high-subsonic speed*, J. Fluid Mech. **43**, 101–145, (2003).

[19] L. Larchevêque, P. Sagaut, I. Mary, O. Labbé. *Large-eddy simulation of a compressible flow past a deep cavity*, Physics of Fluids, **15**, n^o 1, (2003).

[20] N. Bertier, B. Courbet, D. Dutoya, F. Vuillot, P. Sagaut. *Large-eddy simulation of a subsonic flow over a cavity on general unstructured grids*, AIAA paper 2004-0679, 42nd Aerospace Sc. Meeting & exhibit, (2004).

[21] R. Abgrall, T. Sonar, O. Friedrich, G. Billet. *High order approximations for compressible fluid dynamics on unstructured and cartesian meshes*, High-Order Methods for Computational Physics, Lecture Notes in Computational Science and Engineering, Springer, (1999).

[22] G. Billet, O. Louédin. *A simple algorithm to improve the accuracy of TVD-MUSCL schemes,* Inter. Series Num. Math., **129**, 65–75, (1999).

[23] G. Billet, J. Ryan, M. Borrel. *Towards direct numerical simulation of a diffusion flame/shock interaction with an AMR algorithm.* ICCFD 2006.

[24] J.A. Miller, R.E. Mitchell, M.D. Smooke, R.J. Kee. *Toward a comprehensive chemical kinetic mechanism for the oxidation of acetylene: comparison of model predictions with results from flame and shock tube experiments*, Nineteenth symposium on combustion, Combustion Institute , 181–196, (1982).

[25] V. Giovangigli, G. Billet, G. de Gassowski, *Impact of volume viscosity on a shock-diffusion flame interaction,* 11^{th} inter. Conf. Numerical Combustion (SIAM), Granada (2006).